Academia
Quantum

10.20935/AcadQuant8487

Research Article

Unifying liquid water anomalies through a protonic pseudospinor order parameter

Julian G. B. Northey[1,*]

[1] Applied Quantum Physics Branch, Frontier Agri-Science Inc., Ottawa, Canada
* Correspondence: julian.northey@frontieragri.science

Received: 11 May 2026 | **Accepted:** 18 August 2026 | **Published:** 16 September 2026

Abstract

Introduction: Liquid water exhibits correlated density, thermodynamic, dielectric, transport, structural, and phase-boundary anomalies that are commonly described by separate phenomenological variables. This work asks whether a single internal protonic order parameter can provide a common parent architecture for the broader anomaly landscape.

Materials and methods: A local hydrogen-bond unit is represented by the direct product of left/right proton localization and a binary torsional-sign sector, giving a four-component internal protonic pseudospinor. Its bilinear projections define torsional, tetrahedral/crystallinity, and polarization sectors, which are coupled to the hydrodynamic density deviation. These fields enter a Landau–Ginzburg effective Hamiltonian with density–torsion, torsion–crystallinity, and torsion–polarization couplings. The observed equation-of-state density stiffness is distinguished from the bare coefficient of the coupled fluctuation Hamiltonian, and the torsional crossover is rounded at the finite coarse-graining resolution so that its susceptibility remains finite.

Results: The calculations provide sector-level comparisons rather than an independent validation of a common mediator. Density and compressibility are equation-of-state calibration anchors; heat capacity is evaluated with the prescribed rounded torsional stiffness; the broadband dielectric spectra are normalized to the measured 10 GHz loss and use stated temperature-specific composite relaxation times; the isotope-derived memory increment is transferred to viscosity; and the phase branch is a calibrated boundary proxy. Eliminating the centered torsional fluctuation nevertheless derives a rank-one coupling matrix in which density–crystallinity, density–polarization, and crystallinity–polarization cross-responses would share $\chi_q(T) = a_q(T)^{-1}$. No direct mixed cross-response dataset is used here to test that prediction.

Conclusions: The protonic pseudospinor is proposed as an auditable organizing architecture for correlated liquid-water anomalies. Its common four-state origin, bounded admissible state space, and factorized q-mediated coupling structure are the principal theoretical contributions. The rank-one shared-q response is a falsifiable prediction, not a validation established by the present sector-level comparisons. Independent evaluation requires a fully numerical prespecified q-sector and response maps, joint estimation, and held-out measurements of mixed density–polarization, density–crystallinity, or crystallinity–polarization responses.

Keywords: water anomalies; proton tunnelling; spinor order parameter; Landau–Ginzburg theory; dielectric loss; hydrogen-bond network

1. Introduction

Water is anomalous not because it has one unusual property, but because density, thermodynamic, dielectric, dynamical, and phase-boundary observables deviate together from the expectations for ordinary molecular liquids. Finney's historical review frames this as a long-running structural problem in water science, while recent spectroscopy and ultrafast-scattering work sharpen two specific pieces of that problem: nuclear/electronic structure in the hydrogen-bond network and the possible liquid–liquid transition in deeply supercooled water [1–5]. The gap addressed here is therefore not the absence of isolated explanations, but the absence of a compact order parameter that can connect thermodynamic, dielectric, dynamical, and phase-sector behavior within one framework.

Existing models capture important subsets of this behavior. Two-state, locally favored-structure, and liquid–liquid critical-point (LLCP) descriptions connect density and compressibility anomalies to competition between local structures [6, 7]. Recent structural-indicator, finite-size, and large-scale simulation studies further refine how such a transition should be located, interpreted, or challenged in realistic water models [8–13]. These approaches have clarified much of the phenomenology, but they do not by themselves provide a single low-dimensional parent structure that links hydrodynamic density response, protonic/torsional dynamics, polarization, and incipient crystallinity.

A major organizing idea in the literature is that several water anomalies are not independent irregularities, but correlated response-function anomalies. In liquid–liquid and Widom-line descriptions, competition between high-density and low-density local structures links thermodynamic response maxima, structural fluctuations, scattering signatures, and dynamical crossovers [3, 4, 7, 8]. The present work keeps this cluster-based viewpoint, but replaces a purely scalar two-state description by a protonic spinor order parameter whose invariant fields couple density, torsional order, polarization, and incipient crystallinity.

Recent quantum-based work motivates treating protons and local fields as central rather than secondary variables. Advanced vibrational spectroscopy now directly links charge transfer and nuclear quantum effects to the hydrogen-bond network [2]; machine learning and ab initio approaches are extending the accessible scale of electric-field response calculations [14]; field-driven polarization can be thermodynamically distinct from crystallization [15]; electrofreezing simulations report field-induced freezing behavior in bulk water [16]; and high-accuracy free-energy calculations of autoionization emphasize the Grotthuss mechanism and solvent-separated protonic states [17]. These studies are microscopic in character. They do not provide the same kind of bulk coarse-grained phenomenology developed here, but they strongly motivate an effective theory in which proton localization, torsional sign, local fields, and network rearrangement are coupled from the outset.

The proposal in this article is that the minimal coarse-grained carrier of that information is a four-component protonic pseudospinor order parameter. The word "spinor" is used here in a restricted internal-order-parameter sense: the local basis is acted on by Pauli matrices in the proton-localization and torsional-sign subspaces, giving an internal $\mathrm{SU}(2)_\sigma \times \mathrm{SU}(2)_\tau$ algebra. It is not a claim of electronic spin, spinor Bose–Einstein-condensate (BEC) physics, or double-valued transformation under physical spatial rotations. A hydrogen-bond proton supplies a left/right localization degree of freedom in an O–H···O double well. Reorientation about the O···O axis supplies a second binary degree of freedom, represented at the coarse-grained level by a torsional-sign sector. Their direct product gives four local basis states. Coarse-graining the corresponding local amplitudes gives a complex four-component field $\Psi(\vec{r})$, whose physical content is extracted only through bilinears.

The purpose of the paper is not to claim that this construction is a complete microscopic Hamiltonian for liquid water. Rather, the question is deliberately mesoscopic: can Ψ provide a common parent architecture for the anomaly landscape, while representative observables are described transparently through sector-specific calibration and response maps? The model does not compute individual molecular trajectories. It computes thermodynamic and linear-response quantities derived from a continuum effective Hamiltonian for the hydrogen-bond network. Thus the quantum language enters through the local protonic/torsional basis and through the proton-kinetic gradient stiffness, while the working theory is a classical coarse-grained Landau–Ginzburg calculation.

The supplementary materials are organized in explicit numerical order. **Table S1**, **Table S2**, and **Table S3** summarize the field conventions, invariant inventory, and dimensional checks; **Table S4** and **Table S5** give the coefficient inventory and crossover-profile sensitivity; **Table S6** and **Table S7** report the residual audits; **Table S8** lists prospective discriminating tests; and the separate anomaly ledger is **Table S9**. **Figure S1** presents the auxiliary transport comparison. The supplementary derivations are likewise organized sequentially: **Equations (S1), (S2)**, **(S3)**, **(S4)**, **(S5)**, **(S6)**, and **(S7)** define the local unit and gradient scale, **Equations (S8)**, **(S9)**, **(S10)**, **(S11)**, **(S12)**, **(S13)**, **(S14)**, **(S15)**, **(S16)**, **(S17)**, **(S18)**, **(S19)**, **(S20)**, **(S21)**, **(S22)**, **(S23)**, **(S24)**, **(S25)**, and **(S26)** define the bilinears and admissible domain, **Equations (S27)**, **(S28)**, **(S29)**, **(S30)**, **(S31)**, **(S32)**, **(S33)**, **(S34)**, and **(S35)** specify the effective Hamiltonian and coefficient functions, and **Equations (S36)**, **(S37)**, **(S38)**, **(S39)**, **(S40)**, **(S41)**, **(S42)**, **(S43)**, **(S44)**, **(S45)**, **(S46)**, **(S47)**, **(S48)**, **(S49)**, **(S50)**, **(S51)**, **(S52)**, **(S53)**, **(S54)**, **(S55)**, **(S56)**, and **(S57)** give the observable and phase-sector relations.

For the main text, **Equations (1)**, **(2)**, **(3)**, **(4)**, **(5)**, **(6)**, and **(7)** define the local basis and invariant fields; **Equations (8), (9)**, **(10)**, **(11)**, **(12)**, **(13)**, **(14)**, **(15)**, **(16)**, **(17)**, **(18)**, **(19)**, **(20)**, **(21)**, **(22)**, **(23)**, and **(24)** define the Hamiltonian, shared-mediator structure, and coefficient functions; **Equations (25)**, **(26)**, **(27)**, **(28)**, **(29)**, **(30)**, **(31)**, **(32)**, **(33)**, **(34)**, and **(35)** give the comparison formulas and phase-sector proxy; and **Equations (36)**, **(37)**, **(38)**, **(39)**, and **(40)** connect the construction to projected critical scattering and atomistic calibration.

The rest of the paper follows that logic. Section 2 defines the local four-state unit, the invariant fields, the effective Hamiltonian, and the calibration and calculation workflow. Section 3 presents the density/compressibility/dielectric calibration backbone, heat-capacity and broadband dielectric comparisons, the isotope endpoint, and the phase-sector proxy calculation. Section 4 relates the construction to two-state and LLCP descriptions, identifies its phenomenological elements, and states the empirical status and falsification criteria of the shared-q prediction. The separate **Table S9** is a coverage and hypothesis ledger rather than an evidence count; it distinguishes numerical comparisons from mechanistic mappings, contextual associations, and prospective tests.

2. Materials and methods

2.1. Local quantum model and coarse-graining

2.1.1. What exactly is being modeled?

The modeled object is a mesoscopic hydrogen-bond network, not an isolated water molecule and not an atomistic molecular-dynamics trajectory. A local hydrogen-bond unit is assigned two binary variables:

1. proton localization, represented by left/right states $|L\rangle, |R\rangle$ along an O–H···O double well.

2. torsional sign, represented by two inequivalent reorientation sectors $|+\rangle, |-\rangle$ associated with motion about the O···O axis.

This reduced local basis is not intended to replace atomistic descriptions; it is a coarse-grained representation of the protonic and hydrogen-bond degrees of freedom emphasized by recent nuclear-quantum, charge-transfer, and autoionization studies [2, 17]. The local basis is therefore

$$\{|\mathrm{L},+\rangle, |\mathrm{L},-\rangle, |\mathrm{R},+\rangle, |\mathrm{R},-\rangle\} \tag{1}$$

A coarse-grained volume containing many such bonds is described by complex amplitudes in this four-state manifold,

$$\Psi(\vec{r}) = \begin{pmatrix} \psi_{\mathrm{L}+}(\vec{r}) \\ \psi_{\mathrm{L}-}(\vec{r}) \\ \psi_{\mathrm{R}+}(\vec{r}) \\ \psi_{\mathrm{R}-}(\vec{r}) \end{pmatrix} \tag{2}$$

The experimentally relevant variables are not the four amplitudes themselves, but rotationally invariant coarse-grained fields constructed from them and from the hydrodynamic density.

2.1.2. A minimal local Hamiltonian

A minimal single-bond Hamiltonian that motivates the four-state structure is

$$\mathcal{H}_{\mathrm{bond}} = \frac{\epsilon}{2}\sigma_z + \frac{\Delta}{2}\sigma_x + \frac{\Omega}{2}\tau_z + u\,\sigma_z\tau_z - \vec{d}\cdot\vec{E} \tag{3}$$

Here $\vec{\sigma}$ acts on the left/right proton-localization subspace, $\vec{\tau}$ acts on the torsional-sign subspace, ϵ is an instantaneous asymmetry of the double well, Δ is the tunnelling splitting, Ω is the torsional-sign bias, u couples proton localization to torsional sector, and $\vec{d}$ is the local dipole. **Equation (3)** is not fitted bond by bond. Its role is to state the microscopic variables whose collective coarse-graining defines Ψ. The calculations below use the effective continuum Hamiltonian of Section 2.2.

2.1.3. Invariant fields

The continuum theory is expressed in terms of the hydrodynamic density and bilinear projections of the four-state field:

$$\Delta\rho(\vec{r}) = \rho(\vec{r}) - \rho_{\mathrm{ref}}(T,P) \tag{4}$$

$$q_{\mathrm{bil}}(\vec{r}) = \Psi^{\dagger}(\vec{r})\Gamma_q\Psi(\vec{r}), \qquad q(\vec{r}) \equiv q_{\mathrm{bil}}(\vec{r}) - \bar{q}(T,P) \tag{5}$$

$$s(\vec{r}) = \Psi^{\dagger}(\vec{r})\Gamma_s\Psi(\vec{r}) \tag{6}$$

$$\vec{P}(\vec{r}) = P_0\,\Psi^{\dagger}(\vec{r})\Gamma_P\Psi(\vec{r}) \tag{7}$$

Here $\Psi^{\dagger}$ denotes the Hermitian adjoint and P_0 fixes the polarization normalization. The full bilinear q_{bil} records the local imbalance between the two torsional-sign sectors. Its homogeneous background $\bar{q}(T,P)$ is selected by the local bond bias and network environment; the centered variable $q = q_{\mathrm{bil}} - \bar{q}$ is the fluctuation field used in the response Hamiltonian. Equivalently, $\bar{q}$ is the value selected by a conjugate torsional source before the fluctuation expansion is made; **Equation (S12)** writes this source-shift relation explicitly. The symmetric

quadratic fluctuation Hamiltonian is therefore not being asked to generate a nonzero background by itself. Background contributions of $\bar{q}$ are absorbed into the reference density, the crystallinity curvature, and the background dielectric susceptibility, whereas the centered q mediates cross-responses. The matrices Γ_q, Γ_s, and Γ_P are given explicitly in the supplementary materials.

The explicit 4×4 representation matrices and bounded bilinear domain are given in **Section S2**. In the diagonal bond-frame sector, a normalized four-state spinor implies probabilities $w_{L+}, w_{L-}, w_{R+}, w_{R-} \geq 0$, equivalently $1 \pm p \pm q_{bil} \pm s \geq 0$ with the correlated signs shown in **Equations (S21)** and **(S22)**. The centered fluctuation q consequently occupies the translated interval allowed by q_{bil} and $\bar{q}$. In the displayed small-amplitude benchmarks these bounds are not used to regularize a singular quadratic theory; the rounded positive torsional stiffness defined below provides local stability, while the bilinear bounds function as admissibility and extrapolation constraints on the parent state space.

The construction from the local four-state basis to the continuum fields is summarized in **Figure 1**.

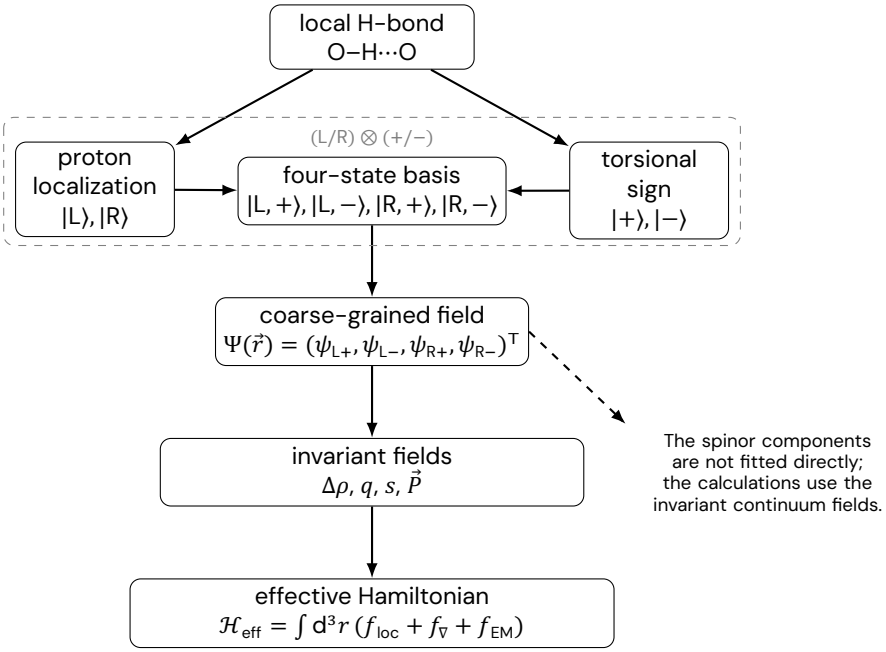

Figure 1. Order-parameter construction. A local hydrogen-bond unit carries proton-localization and torsional-sign information. Their direct product gives a four-state basis, which becomes the four-component coarse-grained field Ψ. Solid arrows indicate the successive construction and coarse-graining steps. The dashed enclosure groups the two local binary factors whose direct product forms the four-state basis, and the dashed arrow points from the spinor amplitudes to the reminder that those amplitudes are not fitted directly. The effective Hamiltonian is instead written in terms of the invariant continuum fields $\Delta\rho$, q, s, and $\vec{P}$.

2.2. Effective Hamiltonian, assumptions, and symmetries

2.2.1. Status of the Hamiltonian

The Hamiltonian used for calculation is an effective mesoscopic fluctuation Hamiltonian,

$$\mathcal{H}_{eff}[\Delta\rho, q, s, \vec{P}] = \int d^3r\, [f_{loc} + f_{\nabla} + f_{EM}] \tag{8}$$

It is not a microscopic electronic Hamiltonian and is not claimed to be an ab initio derivation of water. It is a Landau–Ginzburg Hamiltonian for centered long-wavelength fluctuations about the calibrated homogeneous background. Its assumptions are as follows:

1. The relevant long-wavelength variables are $\Delta\rho$, centered torsional fluctuation q, crystallinity amplitude s, and polarization $\vec{P}$.
2. The free-energy density can be expanded locally in these fields plus leading gradients.
3. Coefficients may depend on T and P, but the same coefficient functions are used across all observables.
4. Only the minimal mixed couplings required to connect density, torsion, crystallinity, and polarization are retained.

2.2.2. Local terms

After the homogeneous torsional background has been absorbed into the reference density, the crystallinity curvature, and the dielectric background, the local fluctuation free energy is

$$f_{\mathrm{loc}} = \frac{1}{2}a_\rho^{(0)}(T,P)(\Delta\rho)^2 + \frac{1}{2}a_q(T)q^2 + \frac{1}{2}A_s(T,P)s^2 + \frac{1}{4}b_s s^4 + \lambda_{\rho q}\Delta\rho\, q + \lambda_{qs}qs^2 + g_{qP}q|\vec{P}|^2 \tag{9}$$

Here $a_\rho^{(0)}$ is the bare density coefficient of the coupled fluctuation Hamiltonian, whereas the observed relaxed density stiffness is defined below. The background crystallinity curvature is $A_s(T,P) = a_s(T,P) + 2\lambda_{qs}\bar{q}(T,P)$. The first line contains the independent sector costs; the second contains the centered fluctuation couplings. The term $\lambda_{\rho q}\Delta\rho q$ mediates density–torsion response, $\lambda_{qs}qs^2$ couples torsional fluctuations to crystallinity, and $g_{qP}q|\vec{P}|^2$ couples them to polarization. The associated background shifts proportional to $\bar{q}$ are not counted a second time in **Equation (9)**.

The torsional bilinear is treated as an internal scalar branch coordinate of the hydrogen-bond network, not as an externally imposed pseudoscalar. The centered expansion therefore permits the displayed mixed terms. A linear term in the full bilinear is equivalent to the conjugate source that selects $\bar{q}(T,P)$; it disappears from the fluctuation Hamiltonian by construction. **Section S2** gives the invariant inventory and states explicitly which higher-order terms are omitted rather than forbidden.

2.2.3. Gradient and electromagnetic terms

The leading gradient terms are

$$f_\nabla = c_1|\nabla\Delta\rho|^2 + \beta_{\mathrm{eff}}|\nabla q|^2 \tag{10}$$

where proton kinetics fixes

$$\beta_{\mathrm{eff}} = \frac{\hbar^2}{8m_{\mathrm{p}}\ell_0^3} = 3.71\times10^{-14}\ \mathrm{J\,m^{-1}} \tag{11}$$

For $\ell_0 = 2.82$ Å, the corresponding high-frequency torsional modulus is $G_q = \beta_{\mathrm{eff}}/\ell_0^2 = 4.66\times10^5$ Pa. The electromagnetic sector is

$$f_{\mathrm{EM}} = \frac{|\vec{P}|^2}{2\chi_{\mathrm{bg}}} - \vec{P}\cdot\vec{E} \tag{12}$$

where $\chi_{\mathrm{bg}}^{-1} = \chi_0^{-1} + 2g_{qP}\bar{q}$ is the polarization stiffness after the homogeneous torsional background is absorbed, and $\vec{E}$ is the applied electric field. The centered coupling $g_{qP}q|\vec{P}|^2$ remains in **Equation (9)**.

2.2.4. Immediate consequences and density–stiffness convention

At quadratic order the centered $(\Delta\rho, q)$ sector is Gaussian. Completing the square gives

$$\frac{1}{2}a_\rho^{(0)}(\Delta\rho)^2 + \lambda_{\rho q}\Delta\rho q + \frac{1}{2}a_q q^2 = \frac{1}{2}a_\rho^{(0)}\left(\Delta\rho + \frac{\lambda_{\rho q}}{a_\rho^{(0)}}q\right)^2 + \frac{1}{2}\left(a_q - \frac{\lambda_{\rho q}^2}{a_\rho^{(0)}}\right)q^2 \tag{13}$$

Equivalently, relaxing the torsional fluctuation at fixed long wavelength gives

$$a_\rho^{\mathrm{rel}}(T,P) = a_\rho^{(0)}(T,P) - \frac{\lambda_{\rho q}^2}{a_q(T)} \equiv a_\rho^{\mathrm{EOS}}(T,P), \qquad a_\rho^{(0)} = a_\rho^{\mathrm{EOS}} + \frac{\lambda_{\rho q}^2}{a_q} \tag{14}$$

Thus the observed, relaxed equation-of-state (EOS) stiffness derived from the International Association for the Properties of Water and Steam 1995 formulation (IAPWS–95) [18] is used in the compressibility plot, rather than treating it as the bare coefficient and reapplying the same correction. The convention prevents double counting and gives $a_\rho^{(0)}a_q - \lambda_{\rho q}^2 = a_\rho^{\mathrm{EOS}}a_q > 0$ whenever the rounded torsional stiffness is positive.

Minimization with respect to density at fixed centered torsional fluctuation gives the linear response

$$\Delta\rho = -\frac{\lambda_{\rho q}}{a_\rho^{(0)}}q + \cdots \tag{15}$$

This relation describes a fluctuation or externally driven density shift; it is not used to regenerate the IAPWS background density curve from a symmetric quadratic Hamiltonian. Its thermal derivative is

$$\left(\frac{\partial\Delta\rho}{\partial T}\right)_P = -\frac{\partial}{\partial T}\left[\frac{\lambda_{\rho q}q + \cdots}{a_\rho^{(0)}(T,P)}\right]_P \tag{16}$$

and is used only when the centered torsional response is explicitly driven, as in a prospective nonequilibrium extension of the framework.

2.2.5. Shared q-mediated coupling structure

The strongest distinction between the present construction and a completely unconstrained multivariable Landau fit is not that the displayed monomials are impossible to write otherwise. It is that density, crystallinity, and polarization couple to the same centered fluctuation of one spinor-derived torsional bilinear. This produces a shared mediator rather than three unrelated pairwise coefficients.

At fixed T and P, the centered q-dependent local part of **Equation (9)** is

$$f_q = \frac{1}{2}a_q q^2 + q\,J_q, \qquad J_q = \lambda_{\rho q}\Delta\rho + \lambda_{qs}s^2 + g_{qP}|\vec{P}|^2 \tag{17}$$

The stationary fluctuation is

$$q_* = -\frac{J_q}{a_q} \tag{18}$$

and substituting it back gives

$$f_q^{\text{eff}} = -\frac{1}{2a_q}\left(\lambda_{\rho q}\Delta\rho + \lambda_{qs}s^2 + g_{qP}|\vec{P}|^2\right)^2 \tag{19}$$

Thus the induced density–crystallinity, density–dielectric, and crystallinity–dielectric cross-couplings are not independent at this order:

$$f_q^{\text{eff}} \supset -\frac{\lambda_{\rho q}\lambda_{qs}}{a_q}\Delta\rho\, s^2 - \frac{\lambda_{\rho q}g_{qP}}{a_q}\Delta\rho|\vec{P}|^2 - \frac{\lambda_{qs}g_{qP}}{a_q}s^2|\vec{P}|^2 \tag{20}$$

A generic Landau expansion could assign these three induced coefficients independently. In the present theory they factor through the same finite torsional susceptibility,

$$\chi_q(T) = a_q(T)^{-1} \tag{21}$$

The corresponding induced coupling matrix is an outer product and therefore has rank one at the retained order. This is the falsifiable mathematical content of the shared q-sector proposal: cross-responses involving density–polarization, density–crystallinity, or crystallinity–polarization mixing should share the same rounded $a_q(T)^{-1}$ profile unless higher-order, nonlocal, or additional mediator sectors are required.

The present benchmark set does not measure any of these mixed cross-responses directly. **Equations (19)**, **(20)** and **(21)** therefore define a structural prediction of the model rather than an empirical validation supplied by the figures below. A decisive evaluation would require a fully numerical prespecified q-sector and response maps, joint estimation on a calibration set, and held-out measurements of at least two independent mixed-response channels.

2.3. Parameter determination and calculation workflow

2.3.1. Calibration philosophy

The analysis accounts separately for four classes of quantities: state-function inputs fixed by accepted equations of state or physical constants; coefficients and effective combinations entering **Equation (9)**; auxiliary response-shape quantities that map those sectors to a particular frequency-domain or transport observable; and derived comparison quantities. Only the first two classes define the static Hamiltonian. The current figures do not constitute a single global fit in which all response maps are prespecified and estimated jointly; the observable-specific quantities are therefore listed explicitly.

This separation between state-function anchoring, bulk-sector specification, auxiliary response maps, and sector-level comparisons is essential. Quantities such as $a_\rho^{\text{EOS}}(T,P)$, which is tied directly to IAPWS–95, are not out-of-sample predictions. Likewise, the broadband dielectric spectra use measured 10 GHz normalization and separately stated composite relaxation times. The current question is therefore organizational rather than confirmatory: can the same parent field architecture be stated consistently across observables usually assigned to separate anomaly families, while the rank-one mixed-response structure is retained as a future direct test?

2.3.2. Coefficient functions

The observed long-wavelength density stiffness is computed from IAPWS–95 [18]; the corresponding bare coefficient in the coupled fluctuation Hamiltonian is then defined by the no-double-counting relation

$$a_\rho^{\mathrm{EOS}}(T,P) = \frac{1}{\rho^2(T,P)\kappa_T(T,P)}, \qquad a_\rho^{(0)}(T,P) = a_\rho^{\mathrm{EOS}}(T,P) + \frac{\lambda_{\rho q}^2}{a_q(T)} \tag{22}$$

The torsional coefficient is represented by a rounded real-valued crossover profile,

$$\begin{aligned} a_q(T) &= a_{q0}\, r(T)^{\mu_q}\left[1 - 0.24\, r(T)^{\Delta_q}\right], \qquad \mu_q = 1.18, \quad \Delta_q = 0.55, \\ r(T) &= \sqrt{x(T)^2 + \delta_x^2}, \qquad x(T) = \frac{T - T_{\mathrm{W}}}{T_{\mathrm{W}}}, \\ \delta_x &= \frac{\Delta T_{\mathrm{round}}}{T_{\mathrm{W}}}, \qquad \Delta T_{\mathrm{round}} = 2\ \mathrm{K}, \qquad T_{\mathrm{W}} = 308.15\ \mathrm{K}. \end{aligned} \tag{23}$$

The 2 K rounding scale is fixed to the finite crossover-resolution window used in the profile-sensitivity audit; it is not an additional fitted exponent or amplitude. With $a_{q0} > 0$, the bracketed factor remains positive over the 247–333 K calibration interval, so **Equation (23)** has a strictly positive minimum and describes a crossover rather than a thermodynamic critical point. It keeps q_*, the induced cross-couplings, the dielectric relaxation map, and the Gaussian Hessian finite throughout the plotted stable-liquid range. The displayed observables identify the normalized crossover only through composite response-map factors; accordingly, the rounded profile is normalized at the same reference temperature and the finite-resolution observable curves are retained. The 2 K scale should therefore be read as a regularization convention fixed by the resolution of the present calibration, not as an independently measured critical width.

The nominal shape exponents were selected by least-squares calibration to the combined dielectric/crossover objective and are held fixed in subsequent calculations [3, 4, 7, 19, 20]. They are strongly covariant because the broadband spectra identify the composite relaxation map more directly than either exponent. **Section S3.4** therefore reports one-at-a-time profile-sensitivity ranges rather than independent Gaussian errors. With the rounded profile evaluated over 247–333 K and a 2% root-mean-square log-profile tolerance, $\mu_q = 1.18$ has range 1.16–1.20, whereas $\Delta_q = 0.55$ remains weakly identified, with range 0.05–1.20. These are effective crossover-shape ranges, not universal critical-exponent confidence intervals.

The bare crystallinity coefficient is written

$$a_s(T,P) = a_{s0} + a_{s1}(T - 273.15) + \nu_s P \tag{24}$$

while the background curvature used in the phase-sector proxy is $A_s = a_s + 2\lambda_{qs}\bar{q}$. The present phase anchors identify this effective branch and its slope combinations, not a_{s0}, a_{s1}, ν_s, b_s, and $\bar{q}$ separately. **Table 1** is therefore a parameter-and-identifiability ledger rather than a claim that every internal factor has an independently measured numerical value.

The figures use the following literature/reference inputs. Ambient-pressure density points are taken from Kell and Smith–Keyes [21, 22]; compressibility data are taken from Millero and from Speedy–Angell [23, 24]; the near-10 GHz dielectric-loss anchor uses Bertolini et al., and the broader GHz–THz spectrum uses the Ellison supplementary-data compilation distributed through the Electronic Physics Auxiliary Publication Service

(EPAPS) [19, 20]; the heat-capacity comparison uses Osborne et al., Angell–Oguni–Sichina, and Archer–Carter [25–27]; and the phase-sector anchors use high-pressure ice and amorphous-ice literature on ice VI–ice VII–water equilibria, amorphization, and low-density amorphous (LDA)–high-density amorphous (HDA) polyamorphism [28–30]. The supplementary transport comparison uses the Brillouin-linewidth benchmark of Koestel and Walther [31].

Table 1. Parameter and identifiability ledger.

Class	Quantity	Value or implementation	Fixed by/data role	Status
EOS input	$a_\rho^{\mathrm{EOS}}(T,P)$	$[\rho^2\kappa_T]^{-1}$	IAPWS–95 density and compressibility	observed relaxed stiffness
Core bulk	$a_\rho^{(0)}(T,P)$	$a_\rho^{\mathrm{EOS}}+\lambda_{\rho q}^2/a_q$	bare coefficient required by the coupled Gaussian convention	derived; not refitted
Core bulk	$a_q(T)$	**Equation (23)**; $\Delta T_{\mathrm{round}}=2$ K; $\mu_q=1.18$ (1.16–1.20), $\Delta_q=0.55$ (0.05–1.20)	dielectric/crossover profile	rounded, calibrated shape
Background	$\bar{q}(T,P)$	homogeneous torsional-bilinear background; absorbed into ρ_{ref}, A_s, and χ_{bg}	local bias/network environment and phase/dielectric background	not separately identifiable
Core bulk	$A_s(T,P)$	$A_s=a_s+2\lambda_{qs}\bar{q}$	high-pressure phase-boundary and amorphous-density anchors	effective curvature and slope combinations identified
Stabilization/ normalization	$a_{q0}, a_{s0}, a_{s1}, v_s, b_s$	$b_s>0$ stabilizes the even-quartic sector, but its magnitude and the remaining internal factors are not separately recovered	only normalized a_q, $A_s=0$, and slope combinations enter	signs/effective combinations only; magnitudes underidentified
Core bulk	$\lambda_{\rho q}$	1.45×10^5 J kg^{-1}	adopted density–torsion response normalization; **Figure 2** itself is an EOS-backed anchor	not independently identified by the EOS curve
Core bulk	λ_{qs}	1.9×10^6 J m^{-3}	phase/amorphous-sector normalization	identified only through effective phase combinations
Core bulk	g_{qP}	1.9×10^{-3} J m C^{-2}	near-10 GHz dielectric-loss scale	calibrated normalization
Derived prediction	$K_{\mathrm{ind}}=-a_q^{-1}\vec{\lambda}\,\vec{\lambda}^{\mathrm{T}}$	rank one at the retained order	no direct mixed density–polarization, density–crystallinity, or crystallinity–polarization dataset is used	untested structural prediction
Core bulk	c_1	1.5×10^{-10} J m^5 kg^{-2}	density-gradient regularization scale	calibrated once
Constant	β_{eff}	$\hbar^2/(8m_{\mathrm{p}}\ell_0^3)$; $\beta_{\mathrm{eff}}/\ell_0^2=4.66\times10^5$ Pa	constants and $\ell_0=2.82$ Å	constant-fixed
Dielectric background	χ_{bg}, P_0	absorbed into dielectric amplitude/normalization; no independent extraction from **Figure 3**	linear-response normalization	not separately identifiable
Dielectric map	α_ε	0.926 in the displayed GHz–THz spectra	common Cole–Cole-type broadening	auxiliary shape

Table 1. *Cont.*

Class	Quantity	Value or implementation	Fixed by/data role	Status
Dielectric map	τ_{eff}	16.06, 7.61, 3.89 ps at 4, 25, 50 °C	effective relaxation map entering **Figure 3**	auxiliary map
Dielectric map	$C_{\varepsilon}, \nu_{\varepsilon}$	not separately identifiable; absorbed into $\tau_{\mathrm{eff}}(T)$ unless an external $\tau_{\mathrm{HB}}(T)$ normalization is imposed	factorized representation in **Equation (30)**	auxiliary factorization
Transport map	α	0.62	stretched-memory exponent in the extended transport kernel	auxiliary shape
Transport map	$\Gamma_0(T)$	smooth tabulated amplitude in the archived transport input	viscosity curve in **Figure S1**	auxiliary map
Transport map	C_{B}	effective prefactor represented by the archived thermal-conductivity model-output curve	Bridgman-type closure	auxiliary map; not separately identified in the present archive
Isotope endpoint	ϵ_{D}	$\ln(10.4/8.3) = 0.22555$; $RT\epsilon_{\mathrm{D}} = 0.559$ kJ mol^{-1}	literature Debye-time ratio; then transferred to viscosity	input map/ cross-sector transfer comparison

Core-bulk entries define the static fluctuation Hamiltonian. Auxiliary-map entries convert the static sectors to spectra or transport curves and are not additional thermodynamic order parameters. The rank-one coupling matrix is a derived prediction and is not fitted to direct mixed-response data. EOS: equation of state; IAPWS: International Association for the Properties of Water and Steam.

2.3.3. How figures are generated

The calculation workflow is as follows:

1. Evaluate $\rho(T,P)$, $\kappa_T(T,P)$, and derived thermodynamic quantities from IAPWS–95 where applicable;
2. Evaluate the rounded $a_q(T)$, the effective background coefficients, and the stated couplings in **Table 1**;
3. Minimize or integrate out the required centered fluctuation sectors of **Equation (9)**;
4. Compute the plotted observables: ρ, κ_T, heat capacity, dielectric loss, transport quantities, or phase-sector slopes;
5. Compare with published experimental/reference datasets using the parameter and response-map roles reported in **Table 1**.

No atomistic numerical simulation is used to generate the thermodynamic, dielectric, phase-sector, or supplementary transport curves. No numerical Mpemba solver or threshold-time comparison is reported in this work.

2.3.4. Quantitative comparison metrics

Quantitative residuals between the plotted model/reference curves and experimental/reference data are summarized in **Table 2**. Root-mean-square error (RMSE), mean absolute error (MAE), mean absolute percentage error (MAPE), maximum absolute error, and signed bias are computed after interpolation of each model curve to the experimental abscissae. The associated reproducibility archive described in the Data Availability statement contains the figure CSV files, the full per-dataset residual table, and scripts used to regenerate these values.

Temperature-resolved broadband dielectric metrics, including a peak-window audit, are reported in **Table S6**. These residuals quantify the individual sector and response-map comparisons; they do not independently test the rank-one mixed-response prediction in **Equation (19)**.

The calibration backbone is shown in **Figure 2**.

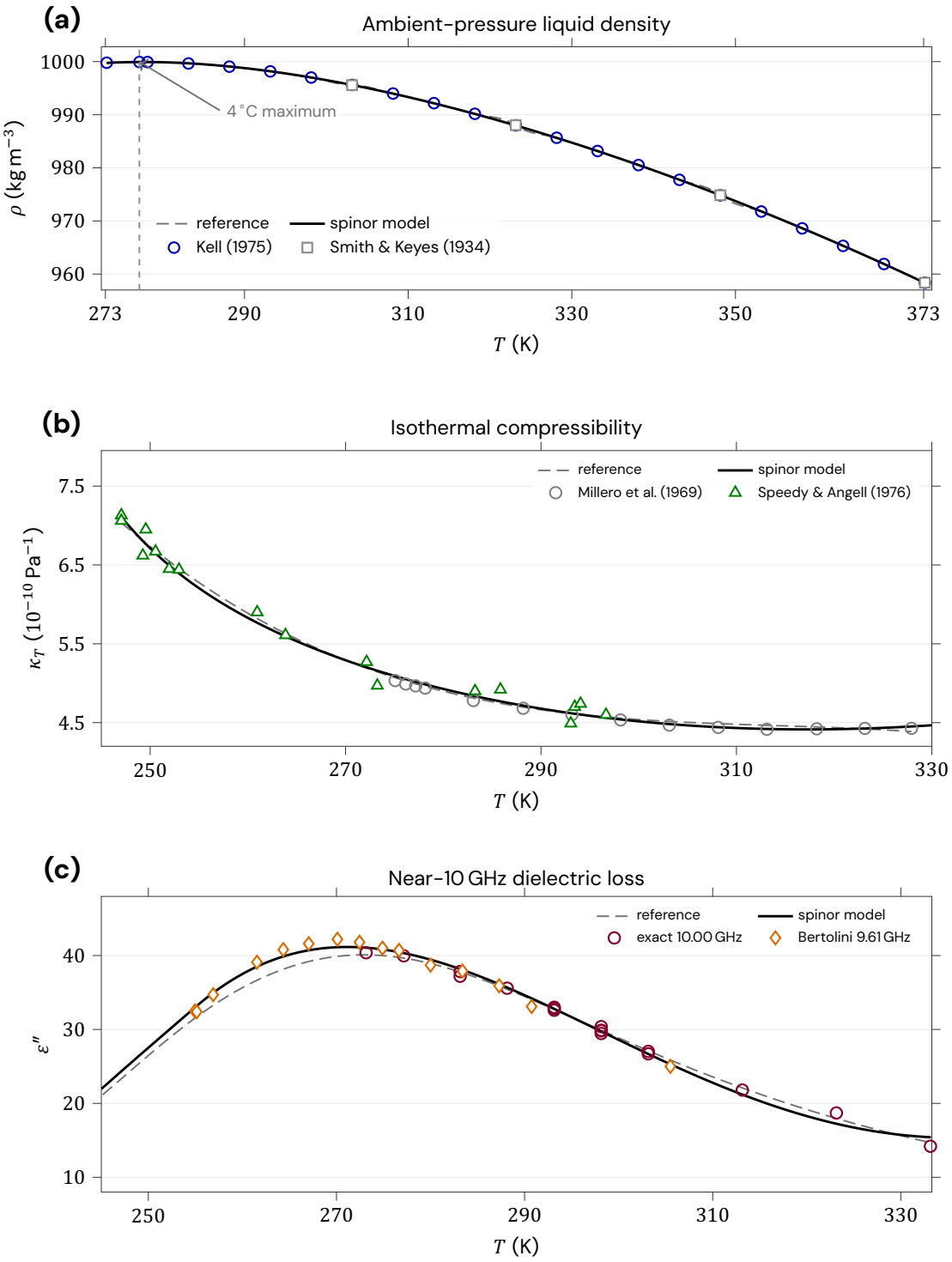

Figure 2. Calibration observables and anchors. Solid curves show the corresponding framework/reference evaluations; dashed curves show the reference compilation used for calibration; symbols show experimental data. (**a**) Ambient-pressure

liquid density from Kell (1975) and Smith & Keyes (1934), including the 4 °C maximum [21, 22]. (**b**) Isothermal compressibility from Millero et al. (1969) and Speedy & Angell (1976), showing the nonmonotonic temperature dependence and the minimum near 46 °C [23, 24]. (**c**) Near-10 GHz dielectric loss from exact 10.00 GHz points and the supercooled 9.61 GHz data of Bertolini et al., showing the broad low-temperature dielectric enhancement [19]. These three observables define the displayed ambient-pressure liquid calibration backbone. The density and compressibility panels are equation-of-state (EOS)-backed calibration anchors rather than independent consequences of the off-diagonal coupling. Phase-boundary and amorphous-density anchors constrain the effective crystallinity-sector combinations described in Table 1. Subsequent figures provide sector-level comparisons for heat capacity, broadband dielectric loss, isotope-sensitive transport, and a derivative phase-boundary proxy; the supplementary materials contain an auxiliary transport comparison. None of these panels directly measures the mixed cross-responses required to test the rank-one mediator.

The broadband dielectric response-map comparison is shown in **Figure 3**.

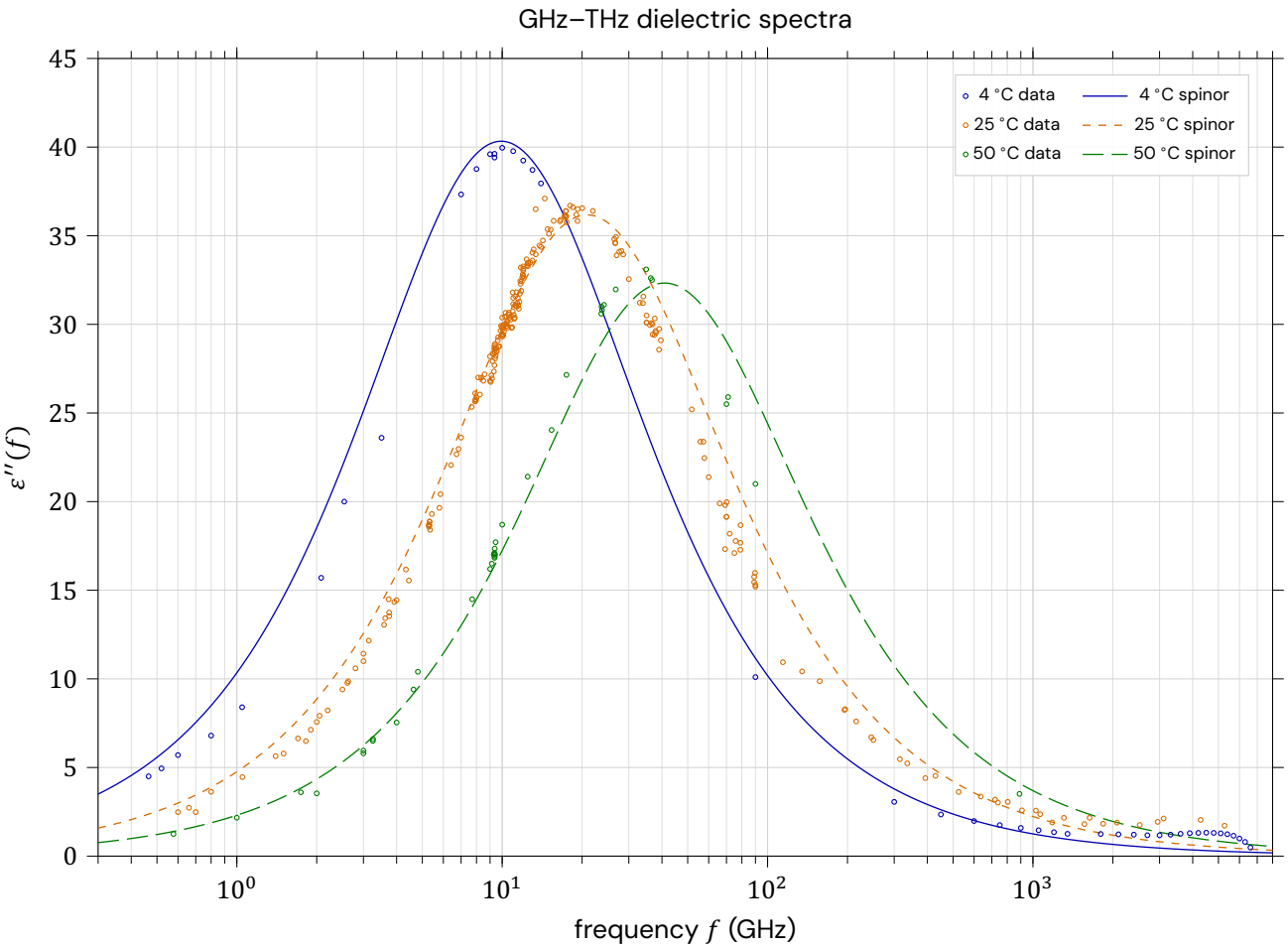

Figure 3. Broadband dielectric-loss response-map comparison. Dielectric-loss spectra are shown as $\varepsilon''(f)$ across the GHz–THz window at 4, 25, and 50 °C. Open symbols are experimental pure-water data from the Ellison supplementary-data compilation distributed through the Electronic Physics Auxiliary Publication Service (EPAPS) [20]. Each plotted curve is normalized to the measured 10 GHz loss and uses the temperature-specific composite τ_{eff} reported in the text, with one common broadening exponent. The comparison therefore assesses the stated dielectric response map without introducing another dielectric order parameter; it is not an independent validation of the shared-q rank-one coupling structure. The construction is given in **Equations (29)** and **(30)**, with details in **Section S4.3**.

Table 2. Aggregate benchmark-error summary for the plotted data.

Figure	Observable	*N*	RMSE	MAE	Max. error	Units
Figure 2a	density	26	0.024	0.021	0.050	kg m^{-3}
Figure 2b	isothermal compressibility	31	0.085	0.063	0.188	10^{-10} Pa^{-1}
Figure 2c	near-10 GHz dielectric loss	32	0.635	0.510	1.457	ε''
Figure 3	GHz–THz dielectric loss	334	1.369	1.008	5.178	ε''
Figure 4	heat capacity	143	0.591	0.345	2.820	J mol^{-1} K^{-1}
Figure 5a	ice VI/VII phase-boundary proxy pressure	41	1.72	1.03	5.92	MPa
Figure 5b	ice VI local boundary-slope proxy	25	0.028	0.019	0.090	MPa K^{-1}
Figure 5c	LDA/HDA density endpoints	2	0.000	0.000	0.000	g cm^{-3}

RMSE: root-mean-square error; MAE: mean absolute error; MAPE: mean absolute percentage error; LDA: low-density amorphous ice; HDA: high-density amorphous ice. RMSE and MAE are reported in the units listed in the final column. For **Figure 3**, the aggregate row is supplemented by temperature-resolved RMSE, MAPE, and peak-window metrics in **Table S6**; this separates absolute spectral error from percentage inflation at low-loss tail points.

The heat-capacity comparison is shown in **Figure 4**.

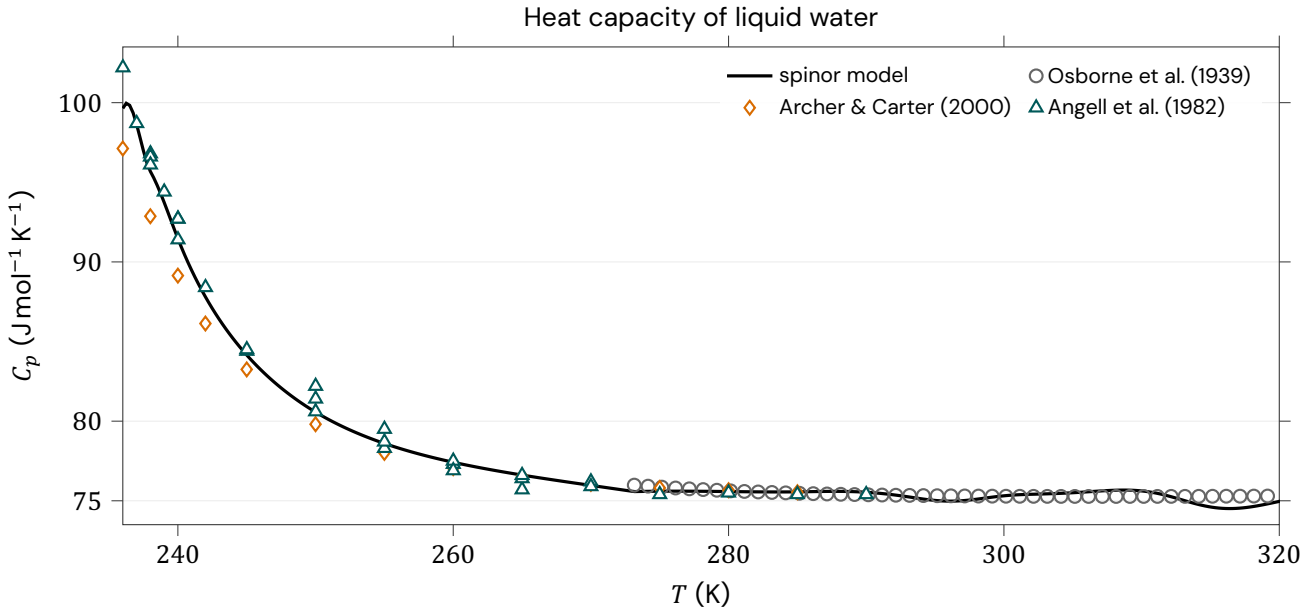

Figure 4. Heat-capacity comparison using the prescribed torsional stiffness. Solid line: framework evaluation of the absolute isobaric heat capacity $C_p(T)$ over 236–320 K. Open circles show stable-liquid benchmark data of Osborne et al. (1939) [25]; diamonds show Archer & Carter (2000) [27]; and triangles show Angell–Oguni–Sichina (1982) [26]. No heat-capacity-specific order parameter is introduced; the stable-liquid excess and deep-supercooled rise follow from the decomposition in **Equation (27)** and the Gaussian torsional fluctuation term in **Equation (28)**, with details in **Section S4.2**. This is a within-sector comparison and does not measure a mixed cross-response of the rank-one coupling matrix.

The calibrated phase-sector proxy and amorphous-density anchors are shown in **Figure 5**.

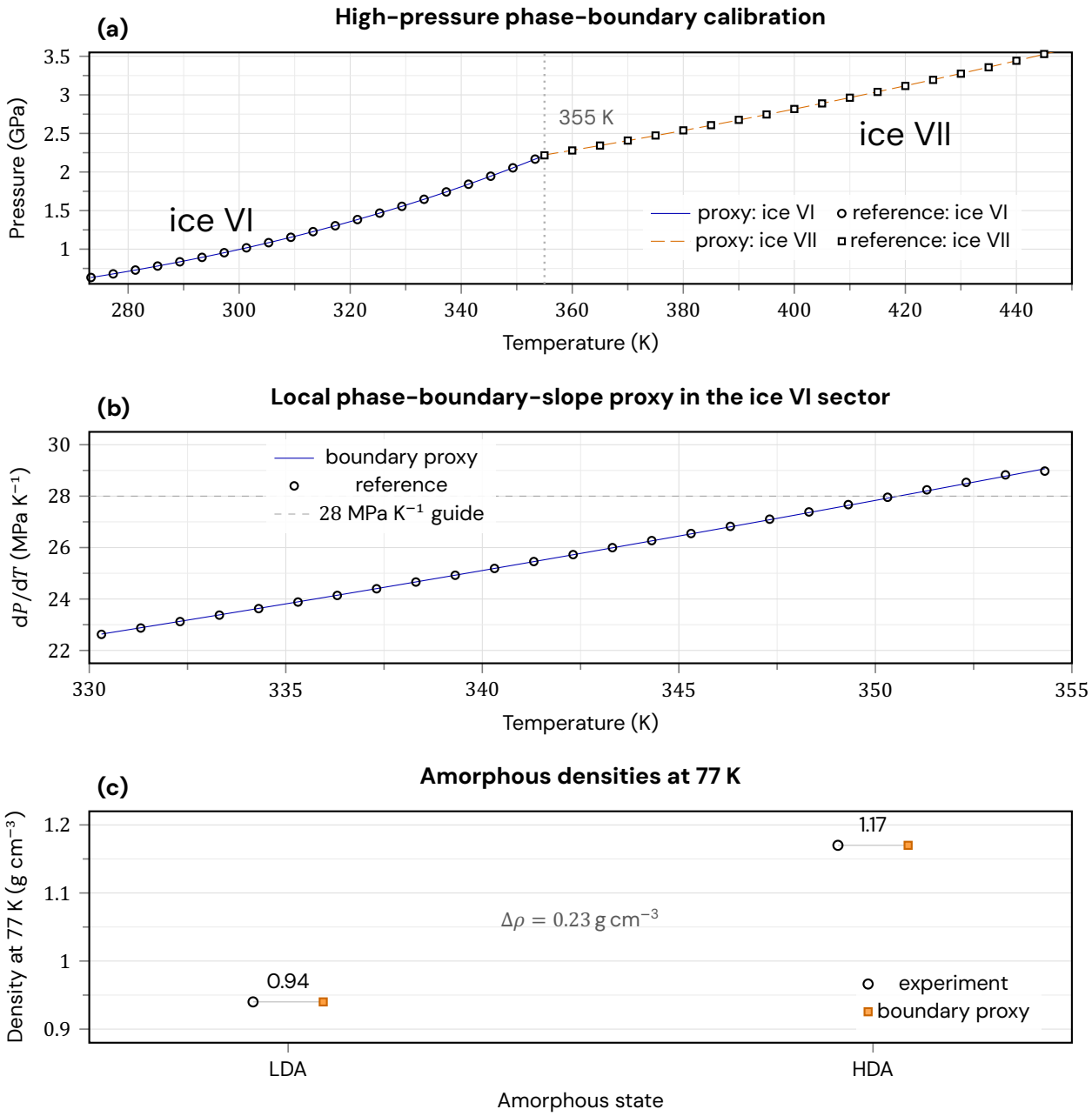

Figure 5. Calibrated phase-sector proxy and amorphous-density anchors. (**a**) High-pressure ice–liquid reference branches for ice VI and ice VII. Open symbols show benchmark coexistence points from the phase-equilibrium literature, whereas the model curves are the calibrated local-instability proxy defined by $A_s = 0$ [28]. The dotted vertical guide marks 355 K, the joining region of the two displayed branches. (**b**) Local phase-boundary-slope proxy in the ice-VI sector. Open circles show slopes extracted from the reference branch; the model curve is the derivative of the calibrated $A_s = 0$ proxy, and the dashed guide marks 28 MPa K^{-1}. It should not be read as an independent first-principles Clausius–Clapeyron derivation. (**c**) Amorphous densities at 77 K for low-density amorphous ice (LDA) and high-density amorphous ice (HDA). Open circles denote experimental anchor values and filled squares denote the adopted framework values. Each thin connector links an experimental anchor to its corresponding framework value; the paired markers are horizontally offset only for visibility [29, 30]. The annotated density contrast is $\Delta\rho = 0.23\,\mathrm{g\,cm^{-3}}$. Plots (**a**,**c**) are calibration/anchor reproductions; plot (**b**) is the derivative evaluation of the same calibrated phase-sector proxy. The minimal even-quartic functional and proxy-slope relations are given in **Equations (32)**, **(33)**, **(34)** and **(35)**.

2.4. Disclosure of AI tool use

During the writing of the manuscript, the AI tool ChatGPT (GPT-5.5.) was used for LaTeX organization, code assistance, and numerical-audit assistance. All AI-assisted output was critically reviewed, verified, and approved by the author, who takes full responsibility for the accuracy, integrity, and final content of the manuscript.

3. Results

The Results are organized as a sequence of calibration anchors and sector-level response-map comparisons involving $\Delta\rho$, q, s, and $\vec{P}$. They assess whether the proposed architecture can be stated consistently across observables usually assigned to separate anomaly families; they are not a cumulative empirical validation of the rank-one shared-q mediator.

3.1. Calibration backbone: density, compressibility, and near-10 GHz dielectric loss

The first benchmark is deliberately limited: it defines the ambient-pressure liquid calibration backbone rather than claiming out-of-sample validation. Density and compressibility are imported through the observed equation-of-state (EOS) background, while the off-diagonal density–torsion coupling defines how centered torsional fluctuations perturb that background and participate in cross-responses. The physical compressibility used in **Figure 2** is therefore

$$\kappa_T(T,P) = \frac{1}{a_\rho^{\mathrm{EOS}}(T,P)\rho^2(T,P)} \tag{25}$$

with the bare coefficient related to a_ρ^{EOS} by **Equation (14)**; the relaxation correction is not applied twice. In the dilute-vapor limit the same EOS density sector gives

$$\alpha_V^{\mathrm{vap}}(T,P) \simeq \frac{P}{T\, a_\rho^{\mathrm{EOS}}(T,P)\rho^2(T,P)} \tag{26}$$

The near-10 GHz observable is the dielectric-loss component ε'' of the complex permittivity. It is used because dielectric spectroscopy in an oscillating field probes phase-lagged polarization response. Thus $\varepsilon'(\omega)$ is the storage response and $\varepsilon''(\omega)$ is the dissipative response. The single-frequency slice in **Figure 2** is a calibration anchor; the broadband comparison below evaluates a separately stated spectral response map.

3.2. Torsional softening in heat capacity and dielectric spectra

A separate sector-level comparison asks whether the prescribed torsional stiffness can be used in observables not reducible to the EOS density anchor. The heat capacity is written as

$$C_p^{\mathrm{model}}(T) = C_p^{(0)}(T) + \Delta C_p^{\mathrm{T}}(T) + \Delta C_p^{\mathrm{crit}}(T) \tag{27}$$

where the last term follows from Gaussian torsional fluctuations,

$$\Delta C_p^{\mathrm{crit}} = -T\frac{\partial^2}{\partial T^2}\left[\frac{k_{\mathrm{B}}TV_{\mathrm{m}}(T)}{2}\int_{|\vec{k}|<k_{\mathrm{max}}}\frac{\mathrm{d}^3k}{(2\pi)^3}\ln\left[\frac{a_q(T)+\beta_{\mathrm{eff}}k^2}{a_*}\right]\right] \tag{28}$$

The reference stiffness a_* makes the logarithm dimensionless and changes only a regular additive background. The cutoff-independent nonanalytic part of the Gaussian fluctuation free energy scales as $a_q^{3/2}$; its second temperature derivative produces the finite calorimetric enhancement. As shown in **Equation (S44)**, $k_{\max}$ changes only regular analytic background terms at the coarse-graining scale ℓ_0.

The resulting absolute heat-capacity comparison is shown in **Figure 4**.

The dielectric spectral extension uses the loss component of the complex permittivity,

$$\varepsilon''(f,T) = \varepsilon''_{10\,\mathrm{GHz}}(T)\frac{\Phi\big(2\pi f\tau_{\mathrm{eff}}(T);\alpha_\varepsilon\big)}{\Phi\big(2\pi(10\,\mathrm{GHz})\tau_{\mathrm{eff}}(T);\alpha_\varepsilon\big)} \tag{29}$$

with

$$\Phi(x;\alpha_\varepsilon) = \left|\mathrm{Im}\left[\frac{1}{1+(\mathrm{i}x)^{\alpha_\varepsilon}}\right]\right|, \qquad \tau_{\mathrm{eff}}(T) = C_\varepsilon\tau_{\mathrm{HB}}(T)\left[\frac{a_q(T_{\mathrm{ref}})}{a_q(T)}\right]^{\nu_\varepsilon} \tag{30}$$

For **Figure 3**, the numerical spectra use the composite relaxation times $\tau_{\mathrm{eff}} = 16.06$, 7.61, and 3.89 ps at 4, 25, and 50 °C, respectively, and each spectrum is normalized to the measured 10 GHz loss. The symbols C_ε and ν_ε provide a factorized interpretation only after a separate $\tau_{\mathrm{HB}}(T)$ normalization is chosen; they are not independently identified by the displayed spectra. Consequently, **Figure 3** evaluates the adequacy of the stated spectral response map but does not independently identify a common q-susceptibility or test the rank-one mixed-response prediction. The full-spectrum RMSE values are 1.203, 1.383, and 1.452 in ε'' at 4, 25, and 50 °C, respectively. At 4 °C the full-spectrum MAPE of 32.6% is dominated by low-loss tail normalization; within one decade on either side of the observed loss maximum, MAPE decreases to 7.13% (RMSE 1.768). Because absolute ε'' values are larger near the peak, peak-window RMSE need not be smaller than full-spectrum RMSE; the reduced peak-window MAPE is the relevant indication that the elevated percentage error is concentrated in the low-loss tail. The complete temperature-resolved audit is given in **Table S6**.

3.3. Isotope endpoint as a cross-sector transfer comparison

An isotope endpoint provides two quantities with different evidentiary status. At 298.15 K, the literature H_2O/D_2O Debye-time endpoints $\tau_{\mathrm{H}} \simeq 8.3$ ps and $\tau_{\mathrm{D}} \simeq 10.4$ ps imply

$$\epsilon_{\mathrm{D}} = \ln\left(\frac{\tau_{\mathrm{D}}}{\tau_{\mathrm{H}}}\right) = 0.22555, \qquad \Delta\ln f_{\mathrm{pk}} = -0.22555 \tag{31}$$

so that the characteristic dielectric-loss peak shifts from $f_{\mathrm{pk,H}} \simeq 19.18$ GHz to $f_{\mathrm{pk,D}} \simeq 15.30$ GHz [32]. Interpreted as a collective memory increment, this corresponds to $\Delta E_{\mathrm{act}}^{(\mathrm{D})} = RT\epsilon_{\mathrm{D}} = 0.559$ kJ mol^{-1}, not to a bare O–H/O–D bond-energy difference. Using the same memory increment in the transport closure gives $\ln(\eta_{\mathrm{D}}/\eta_{\mathrm{H}})_{\mathrm{pred}} = 0.2234$, compared with the room-temperature endpoint value $\ln(1.097/0.890) = 0.2091$, a residual of 0.0143 log units, or about 1.4% in the viscosity ratio [33]. The dielectric peak migration is therefore an algebraic mapping of literature Debye-time inputs, not an independent test of the spinor sector. The nontrivial component is the viscosity transfer comparison: the dielectric-derived memory increment is propagated through the transport closure without refitting to the D_2O viscosity endpoint. This comparison evaluates the dielectric-to-transport memory closure; it does not test the static rank-one density–crystallinity–polarization mediator. **Table 3** separates these evidentiary roles explicitly.

Table 3. Isotope endpoint at 298.15 K, with the evidentiary status of each comparison stated explicitly.

Quantity	Input or observation	Derived value/model result	Evidentiary role
Dielectric peak migration	Literature endpoints $\tau_H = 8.3$ ps and $\tau_D = 10.4$ ps	f_{pk}: 19.18 → 15.30 GHz; $\Delta \ln f_{pk} = -0.22555$	Input-derived algebraic mapping through $f_{pk} = (2\pi\tau)^{-1}$; not an independent test of the spinor sector
Viscosity isotope ratio	Observed $\ln(\eta_D/\eta_H) = 0.2091$	Predicted 0.2234 from the same dielectric-derived memory increment; residual 0.0143	Held-out cross-sector transfer comparison for the dielectric-to-transport closure; not a test of the static rank-one mediator

3.4. Phase-sector coupling and local boundary proxy

The even-quartic crystallinity sector about the homogeneous torsional background is

$$f_{\text{solid}} = \frac{1}{2}A_s(T,P)s^2 + \frac{1}{4}b_s s^4 \tag{32}$$

with

$$A_s(T,P) = a_s(T,P) + 2\lambda_{qs}\bar{q}(T,P) \tag{33}$$

For $b_s > 0$, the condition $A_s = 0$ is the local loss-of-stability or ordering-onset line of this minimal even-quartic sector. It is not, by itself, a derivation of first-order ice–liquid coexistence. In **Figure 5** it is used as a calibrated local phase-boundary proxy against the reference melting branches. Implicit differentiation gives the proxy slope

$$\frac{\mathrm{d}P}{\mathrm{d}T} = -\frac{\partial_T A_s}{\partial_P A_s} = -\frac{\partial_T[a_s + 2\lambda_{qs}\bar{q}]}{\partial_P[a_s + 2\lambda_{qs}\bar{q}]} \tag{34}$$

For the displayed ice-VI segment, the evaluated curve uses the local approximation $\partial_P \bar{q} \simeq 0$, so that

$$\frac{\mathrm{d}P}{\mathrm{d}T} \simeq -\frac{\partial_T[a_s + 2\lambda_{qs}\bar{q}]}{\nu_s} \tag{35}$$

A non-negligible measured value of $(\partial\bar{q}/\partial P)_T$ would enter the denominator of **Equation (34)**. A genuine first-order coexistence calculation would additionally require a free-energy form with two competing minima and equality of their Gibbs free energies; that extension is not inferred from $A_s = 0$ here. The reference branch, derivative proxy, and amorphous-density anchors are shown in **Figure 5**.

4. Discussion

4.1. What the model organizes and derives

The central contribution is a proposed parent field architecture and the rank-one mixed-response structure derived from it. The density and compressibility curves define the EOS-backed calibration background; heat capacity is compared using the prescribed rounded torsional stiffness; the dielectric spectra use an explicitly stated auxiliary response map; the isotope endpoint evaluates a dielectric-to-transport transfer; and the high-pressure calculation is a calibrated crystallinity-boundary proxy. These comparisons establish sector-level compatibility with the architecture, not independent validation of a common mediator. The reduced theory has

Landau form, but the spinor construction supplies a common bilinear origin, a bounded parent domain, and a specific factorized q-mediated response prediction.

4.2. Scope of the anomaly claim

The calculations presented here are calibration anchors and sector-level comparisons; they do not define the full intended scope of the framework or validate the shared mediator. **Table S9** catalogues 75 anomaly entries. Of these, 52 (69.3%) are explicitly classified as ledger-only contextual mappings, and the Mpemba entry is classified separately as a prospective nonequilibrium extension with no numerical comparison. The remaining entries include calibration anchors, derived evaluations, response-map comparisons, and conceptual projections. The claim is therefore not that every catalogued anomaly has been fitted or predicted, but that the catalogue can be organized as a research program within one proposed parent architecture.

This distinction separates taxonomic coverage from empirical validation. The current data do not independently determine the density–polarization, density–crystallinity, or crystallinity–polarization cross-responses required to test the outer-product matrix in **Equation (19)**. Such a test would require a fully numerical shared q-sector and response maps prespecified before fitting, a single joint calibration, and held-out direct cross-response data. Until that program is completed, the rank-one relation is a falsifiable prediction of the architecture rather than an experimentally established result.

4.3. Relation to two-state, locally favored-structure, and LLCP descriptions

The present framework is best viewed as a parent order-parameter formulation for two-state and liquid–liquid critical-point descriptions. In this interpretation, the familiar high-density-liquid (HDL)–low-density-liquid (LDL) scalar coordinate is not rejected, but embedded as a lower-dimensional projection of the spinor-derived sectors $\Delta\rho$, q, and s. Existing LLCP, Widom-line, and locally favored-structure approaches show that density, compressibility, heat capacity, and dynamical crossovers can be organized by emergent scalar structural modes [6–10]. In the present theory, these scalar descriptions are interpreted as lower-dimensional projections of the spinor-derived fields rather than as competing order parameters.

A useful way to state the connection is that an effective liquid–liquid coordinate may be written schematically as **Equation (36)**:

$$m_{\mathrm{LL}} = c_\rho\,\Delta\rho + c_q\,q + c_s\,s \tag{36}$$

where the coefficients depend on the observable being probed. Density and wide-angle X-ray scattering (WAXS)-like observables primarily project onto $\Delta\rho$ and s, dielectric-loss observables project onto q and $\vec{P}$, and calorimetric response is sensitive to the softening of $a_q(T)$ through the coupled fluctuation sector. In this sense, the spinor order parameter is not introduced to discard the two-state picture, but to provide a parent mesoscopic variable from which density-like, structural, torsional, and polarization observables can be obtained as different projections.

Recent pump–probe scattering studies, perspective articles, and large-scale simulations of deeply supercooled water further clarify what remains outside the scope of the present calculation. Reports of high-density-liquid (HDL)–low-density-liquid (LDL) conversion, small-angle X-ray scattering (SAXS) enhancement, LLCP-like critical behavior, phase coexistence, or alternative decompression interpretations require explicit treatment of scattering intensities, correlation lengths, finite domains, and crystallization pathways [3–5, 10, 12, 13]. The present

work does not claim to compute those time-resolved WAXS/SAXS signals directly. Instead, it establishes the lower-dimensional bulk Hamiltonian and its thermodynamic, dielectric, and phase-sector projections.

The projected-coordinate connection to conventional critical scattering is direct at Gaussian order. Let $\vec{\phi} = (\Delta\rho, q, s)^{\mathsf{T}}$ and $m_{\mathrm{LL}} = \vec{c}^{\mathsf{T}}\vec{\phi}$. Expanding about a homogeneous state gives

$$F_2 = \frac{1}{2}\sum_{\vec{k}} \vec{\phi}(-\vec{k})^{\mathsf{T}} \left[A + Kk^2\right] \vec{\phi}(\vec{k}) \tag{37}$$

so the projected structure factor is

$$S_{\mathrm{LL}}(k) = \langle |m_{\mathrm{LL}}(\vec{k})|^2 \rangle = k_{\mathrm{B}}T\, \vec{c}^{\mathsf{T}} \left[A + Kk^2\right]^{-1} \vec{c} \tag{38}$$

If one soft eigenmode dominates, **Equation (38)** reduces to the Ornstein–Zernike form

$$S_{\mathrm{LL}}(k) \simeq \frac{S_{\mathrm{LL}}(0)}{1 + \xi^2 k^2}, \qquad \xi^2 = \frac{K_{\mathrm{soft}}}{A_{\mathrm{soft}}} \tag{39}$$

Thus LLCP/two-state scattering variables can be treated as projections of the spinor-derived $(\Delta\rho, q, s)$ sector. Computing absolute SAXS/WAXS intensities, Porod domains, or time-resolved conversion pathways remains a future extension rather than a claim of the present benchmark set.

4.4. What remains phenomenological

Several parts of the construction remain phenomenological. The rounded coefficient function $a_q(T)$, the homogeneous background $\bar{q}(T, P)$, and the effective phase curvature $A_s(T, P)$ are not derived from an ab initio electronic Hamiltonian. The dielectric spectral comparison uses auxiliary shape parameters and temperature-specific composite relaxation times, and the supplementary transport curves use additional response-layer closures. These features define the model's present status: it is an effective organizing architecture with a derived, falsifiable rank-one cross-response prediction, not a jointly fitted and independently validated shared-mediator theory.

A natural next step is to compute the mesoscopic coefficients from atomistic or electronic-structure trajectories rather than fitting them at the continuum level. In an ab initio molecular-dynamics (AIMD) or neural-network-potential (NNP) workflow, one would assign local bond-frame projectors corresponding to p_i, q_i, and s_i, coarse-grain them to $\vec{\phi} = (\Delta\rho, q, s, \vec{P})$, estimate the distribution $P(\vec{\phi})$, and recover a local free-energy surface

$$F(\vec{\phi}) = -k_{\mathrm{B}}T \ln P(\vec{\phi}) \tag{40}$$

The stiffness matrix would then follow from the Hessian $A_{ij} = \partial^2 F/\partial\phi_i\partial\phi_j$, while the gradient coefficients could be extracted from the small-k behavior of the corresponding structure-factor matrix. The crystallinity amplitude s can be anchored in such trajectories by regression against a standard local tetrahedrality metric, for example the Errington–Debenedetti orientational order parameter q_{t}, using a near-homogeneous calibration such as $s = C_s(q_{\mathrm{t}} - q_{\mathrm{t}}^{(0)}) + \mathcal{O}[(q_{\mathrm{t}} - q_{\mathrm{t}}^{(0)})^2]$; determining the mapping coefficient C_s is an atomistic calibration problem rather than an additional main-text fit [34]. This route would turn the present mesoscopic closure into a bridge from electronic-structure or machine learning simulations to experimentally measured bulk response.

4.5. Solution, confined, and interfacial extensions

Solution, confined-water, and interfacial studies point to related but distinct extensions. Supercooled aqueous solutions that undergo reversible liquid–liquid-like transitions show that hydrogen-bond spectroscopic states can change discontinuously when crystallization is suppressed [35]. Confined-water work shows that geometry, surface chemistry, and electrostatics reshape hydrogen-bond topology, dielectric response, vibrational spectra, crystallization, and transport [36]. Interfacial simulations likewise connect anomalous surface tension to competing hydrogen-bond orders at and below the surface [37]. Separately, the Mpemba experiments of Tang et al. [38] provide a possible future benchmark for a nonequilibrium extension, as discussed in supplementary **Section S5**; no numerical threshold-time comparison is reported in the present work. The solution, confined-water, and interfacial observations motivate future surface, solute, and boundary-field extensions of the present Hamiltonian, but they are not treated here as direct validations of the bulk parameter set.

4.6. What would falsify the spinor interpretation

The most direct falsification criterion is the mixed-response structure itself. If measured density–polarization, density–crystallinity, and crystallinity–polarization susceptibilities cannot be described by one common rounded $a_q(T)^{-1}$ factor after a single joint calibration, the rank-one shared-mediator proposal fails at the retained order. Additional warning signs would be incompatible temperature dependences in heat-capacity and dielectric response maps, or failure of the calibrated phase proxy once $\bar{q}(T,P)$ is measured directly. **Equation (31)** records the literature-anchored dielectric mapping from 19.18 to 15.30 GHz at 298.15 K; the linked viscosity calculation is a limited held-out transfer comparison, not a test of the static outer-product matrix.

5. Conclusions

This article proposes an internal protonic pseudospinor as an organizing parent order parameter for the anomaly landscape of liquid water. The construction begins from a local four-state hydrogen-bond unit carrying proton-localization and torsional-sign information. Its full torsional bilinear is separated into a homogeneous background and a centered response field; the latter enters a stable, rounded Landau–Ginzburg fluctuation Hamiltonian together with density, crystallinity, and polarization sectors.

The principal theoretical result is the factorized outer-product coupling matrix obtained after eliminating the centered torsional fluctuation. It predicts that direct density–crystallinity, density–polarization, and crystallinity–polarization cross-responses should share one finite susceptibility $\chi_q(T,P) = a_q(T,P)^{-1}$. The present figures do not measure those mixed responses and therefore do not validate the rank-one mediator. Instead, they document EOS anchors, sector-specific response-map comparisons, an isotope-to-transport transfer comparison, and a calibrated phase-boundary proxy.

The framework is intended to organize the anomaly landscape catalogued in **Table S9**, but most ledger entries are contextual or prospective rather than quantitative tests. In particular, the displayed $A_s = 0$ construction is a calibrated local phase-boundary proxy; a first-order coexistence theory would require competing free-energy minima and equality of their Gibbs free energies. The Mpemba anomaly is treated only as a prospective nonequilibrium extension; no numerical threshold-time comparison is presented.

The next decisive step is a prespecified joint analysis of direct mixed-response data. Pressure-dependent dielectric and density measurements, structural/scattering proxies for crystallinity, field-dependent polarization

responses, and direct atomistic estimates of the torsional background could determine whether the inferred cross-coupling matrix is approximately rank one. Failure of those held-out channels to share the predicted $a_q(T,P)^{-1}$ structure would require extension or rejection of the proposed architecture.

Acknowledgments

The author thanks colleagues who provided critical feedback on the development of this manuscript. The author acknowledges the use of the AI tool ChatGPT (GPT-5.5) for language editing, as well as for LaTeX organization, code assistance, and numerical-audit assistance as declared in the Materials and methods section. The tool was applied to enhance clarity and scholarly tone, and all edits were carefully reviewed and validated by the author to ensure accuracy, compliance with academic standards, and research integrity. The author fully supports Academia.edu Journals' adherence to COPE guidelines on AI in publication ethics and confirms that this use has been managed responsibly and ethically.

Funding

This research received no external funding.

Conflict of interest

The author is an employee of Frontier Agri-Science Inc. (Ottawa, Canada). Frontier Agri-Science Inc. played no role in the study's conception, design, execution, or interpretation, or with the writing of this manuscript. The author declares no other financial or personal competing interests.

Data availability statement

The data supporting the findings of this publication has been made available within a publicly accessible repository at https://doi.org/10.5281/zenodo.21361630.

Supplementary materials

The supplementary materials are available at https://doi.org/10.20935/AcadQuant8487. References [39–62] are cited in the supplementary materials.

Publisher's note

Academia.edu Journals stays neutral regarding jurisdictional claims in published maps and institutional affiliations. All claims expressed in this article are solely those of the authors and do not necessarily represent those of their affiliated organizations, or those of the publisher, the editors, and the reviewers. Any product that may be evaluated in this article, or claim that may be made by its manufacturer, is not guaranteed or endorsed by the publisher.

Copyright

© 2026 copyright by the author. This article is an open access article distributed under the terms and conditions of the Creative Commons Attribution (CC BY) license.

References

1. Finney JL. The structure of water: a historical perspective. J Chem Phys. 2024; 160 (6): 060901. doi: 10.1063/5.0182665
2. Flór M, Wilkins DM, de la Puente M, Laage D, Cassone G, Hassanali A, et al. Dissecting the hydrogen bond network of water: charge transfer and nuclear quantum effects. Science. 2024; 386 (6726): Eads4369. doi: 10.1126/science.ads4369
3. Kim KH, Amann-Winkel K, Giovambattista N, Späh A, Perakis F, Pathak H, et al. Experimental observation of the liquid-liquid transition in bulk supercooled water under pressure. Science. 2020; 370 (6519): 978–82. doi: 10.1126/science.abb9385
4. You S, Ladd-Parada M, Nam K, Karina A, Lee S, Shin M, et al. Experimental evidence of a liquid-liquid critical point in supercooled water. Science. 2026; 391 (6792): 1387–91. doi: 10.1126/science.aec0018
5. Paesani F. Catching water's hidden transition. Science. 2026; 391 (6792): 1318–9. doi: 10.1126/science.aef3474
6. Russo J, Tanaka H. Understanding water's anomalies with locally favoured structures. Nat Commun. 2014; 5 (1): 3556. doi: 10.1038/ncomms4556
7. Stanley HE, Kumar P, Xu L, Yan Z, Mazza MG, Buldyrev SV, et al. The puzzling unsolved mysteries of liquid water: some recent progress. Phys A. 2007; 386 (2): 729–43. doi: 10.1016/j.physa.2007.07.044
8. Foffi R, Sciortino F. Correlated fluctuations of structural indicators close to the liquid-liquid transition in supercooled water. J Phys Chem B. 2023; 127 (1): 378–86. doi: 10.1021/acs.jpcb.2c07169
9. Foffi R, Sciortino F. Identification of local structures in water from supercooled to ambient conditions. J Chem Phys. 2024; 160 (9): 094504. doi: 10.1063/5.0188764
10. Sciortino F, Zhai Y, Bore SL, Paesani F. Constraints on the location of the liquid-liquid critical point in water. Nat Phys. 2025; 21 (3): 480–5. doi: 10.1038/s41567-024-02761-0
11. Malek SMA, Sciortino F, Poole PH, Saika-Voivod I. Liquid-liquid phase transition in simulated supercooled water nanodroplets. Phys Rev Lett. 2025; 134 (13): 138001. doi: 10.1103/PhysRevLett.134.138001
12. Wang L-P, Berrens M, Donadio D. Direct observation of liquid-liquid phase coexistence in deeply supercooled water using an accurate polarizable multipole model. Proc Natl Acad Sci USA. 2026; 123 (4): e2526573123. doi: 10.1073/pnas.2526573123
13. Kumar R, de Almeida Ribeiro I, Dhabal D, Molinero V. Rethinking the evidence for a liquid-liquid transition in water: what decompression experiments reveal. J Chem Phys. 2026; 164 (2): 024506. doi: 10.1063/5.0304941
14. Joll K, Schienbein P, Rosso KM, Blumberger J. Machine learning the electric field response of condensed phase systems using perturbed neural network potentials. Nat Commun. 2024; 15 (1): 8192. doi: 10.1038/s41467-024-52491-3

15. Conti Nibali V, Maiti S, Saija F, Heyden M, Cassone G. Electric-field induced entropic effects in liquid water. J Chem Phys. 2023; 158 (18): 184501. doi: 10.1063/5.0139460

16. Cassone G, Martelli F. Electrofreezing of liquid water at ambient conditions. Nat Commun. 2024; 15: 1856. doi: 10.1038/s41467-024-46131-z

17. Dasgupta S, Cassone G, Paesani F. Nuclear quantum effects and the Grotthuss mechanism dictate the pH of liquid water. J Phys Chem Lett. 2025; 16 (12): 2996–3003. doi: 10.1021/acs.jpclett.5c00168

18. International Association for the Properties of Water and Steam. R6-95(2018): Revised release on the IAPWS formulation 1995 for the thermodynamic properties of ordinary water substance for general and scientific use. 2018. Available from: https://iapws.org/documents/release/IAPWS-95

19. Bertolini D, Cassettari M, Salvetti G. The dielectric relaxation time of supercooled water. J Chem Phys. 1982; 76 (6): 3285–90. doi: 10.1063/1.443323

20. Ellison WJ. Permittivity of pure water, at standard atmospheric pressure, over the frequency range 0–25 THz and the temperature range $0–100$ °C. J Phys Chem Ref Data. 2007; 36 (1): 1–18. doi: 10.1063/1.2360986

21. Kell GS. Density, thermal expansivity, and compressibility of liquid water from 0 °C to 150 °C: correlations and tables for atmospheric pressure and saturation reviewed and expressed on 1968 temperature scale. J Chem Eng Data. 1975; 20 (1): 97–105. doi: 10.1021/je60064a005

22. Smith LB, Keyes FG. The volumes of unit mass of liquid water and their correlation as a function of pressure and temperature. Proc Am Acad Arts Sci. 1934; 69: 285–312. doi: 10.2307/20023049

23. Millero FJ, Curry RW, Drost-Hansen W. Isothermal compressibility of water at various temperatures. J Chem Eng Data. 1969; 14 (4): 422–5. doi: 10.1021/je60043a018

24. Speedy RJ, Angell CA. Isothermal compressibility of supercooled water and evidence for a thermodynamic singularity at -45 °C. J Chem Phys. 1976; 65 (3): 851–8. doi: 10.1063/1.433153

25. Osborne NS, Stimson HF, Ginnings DC. Thermal properties of saturated water and steam. J Res Natl Bur Stand. 1939; 23 (2): 261–70. doi: 10.6028/jres.023.009

26. Angell CA, Oguni M, Sichina WJ. Heat capacity of water at extremes of supercooling and superheating. J Phys Chem. 1982; 86 (6): 998–1002. doi: 10.1021/j100395a032

27. Archer DG, Carter RW. Thermodynamic properties of the NaCl + H_2O system. 4. Heat capacities of H_2O and NaCl(aq) in cold-stable and supercooled states. J Phys Chem B. 2000; 104 (35): 8563–84. doi: 10.1021/jp0003914

28. Antsyshkin DV, Dunaeva AN, Kuskov OL. Thermodynamics of phase transitions in the system ice VI-ice VII-water. Geochem Int. 2010; 48 (7): 633–42. doi: 10.1134/S0016702910070013

29. Mishima O, Calvert LD, Whalley E. An apparently first-order transition between two amorphous phases of ice induced by pressure. Nature. 1985; 314: 76–8. doi: 10.1038/314076a0

30. Klotz S, Strässle T, Nelmes RJ, Loveday JS, Hamel G, Rousse G, et al. Nature of the polyamorphic transition in ice under pressure. Phys Rev Lett. 2005; 94 (2): 025506. doi: 10.1103/PhysRevLett.94.025506

31. Koestel D, Walther T. The Brillouin linewidth in water as a function of temperature and salinity: the missing empirical relationship. Appl Phys B. 2024; 130 (4): 53. doi: 10.1007/s00340-024-08189-x

32. Kaatze U. Dielectric relaxation of H_2O/D_2O mixtures. Chem Phys Lett. 1993; 203 (1): 1–4. doi: 10.1016/0009-2614(93)89299-W

33. Assael MJ, Monogenidou SA, Huber ML, Perkins RA, Sengers JV. New international formulation for the viscosity of heavy water. J Phys Chem Ref Data. 2021; 50 (3): 033102. doi: 10.1063/5.0048711

34. Errington JR, Debenedetti PG. Relationship between structural order and the anomalies of liquid water. Nature. 2001; 409 (6818): 318–21. doi: 10.1038/35053024

35. Woutersen S, Ensing B, Hilbers M, Zhao Z, Angell CA. A liquid-liquid transition in supercooled aqueous solution related to the HDA-LDA transition. Science. 2018; 359 (6380): 1127–31. doi: 10.1126/science.aao7049

36. Wang Z. Confined water in low-dimensional materials: structural, spectroscopic, and transport phenomena. Acad Nano. 2026; 3 (1). doi: 10.20935/AcadNano8180

37. Yuan J, Qiu K, Sun G, Tanaka H. Competing hydrogen-bond orders drive water's anomalous surface tension. Nat Commun. 2026; 17 (1): 1498. doi: 10.1038/s41467-026-69356-6

38. Tang Z, Huang W, Zhang Y, Liu Y, Zhao L. Direct observation of the Mpemba effect with water: probe the mysterious heat transfer. InfoMat. 2023; 5 (2): e12352. doi: 10.1002/inf2.12352

39. Chaplin M. Anomalous properties of water. Water Structure and Science; 2020. Available from: https://vitroid.github.io/water-science/water/water_anomalies.html

40. International Association for the Properties of Water and Steam. R14-08(2011): Revised release on the pressure along the melting and sublimation curves of ordinary water substance. 2011. Available from: https://iapws.org/technical-guidance/release/MeltSub

41. National Institute of Standards and Technology. Thermophysical properties of fluid systems. Available from: https://webbook.nist.gov/chemistry/fluid/

42. Wolfenbarger NS, Carnahan E, Jordan JS, Hesse MA. A comprehensive dataset for the thermal conductivity of ice Ih for application to planetary ice shells. Data Brief. 2021; 36: 107079. doi: 10.1016/j.dib.2021.107079

43. Ratcliffe EH. The thermal conductivity of ice: new data on the temperature coefficient. Philos Mag. 1962; 7 (79): 1197–203. doi: 10.1080/14786436208209120

44. Katayama Y, Hattori T, Saitoh H, Ikeda T, Aoki K, Fukui H, et al. Structure of liquid water under high pressure up to 17 GPa. Phys Rev B. 2010; 81 (1): 014109. doi: 10.1103/PhysRevB.81.014109

45. Andersson O. Dielectric relaxation of low-density amorphous ice under pressure. Phys Rev Lett. 2007; 98 (5): 057602. doi: 10.1103/PhysRevLett.98.057602

46. Lock AJ, Bakker HJ. Temperature dependence of vibrational relaxation in liquid H_2O. J Chem Phys. 2002; 117: 1708–13. doi: 10.1063/1.1485966

47. Holten V, Sengers JV, Anisimov MA. Equation of state for supercooled water at pressures up to 400 MPa. J Phys Chem Ref Data. 2014; 43: 043101. doi: 10.1063/1.4895593

48. International Association for the Properties of Water and Steam. R10-06(2009): Revised release on the equation of state 2006 for H_2O ice Ih. 2009. Available from: https://iapws.org/technical-guidance/release/Ice-2009

49. Mallamace F, Corsaro C, Broccio M, Branca C, González-Segredo N, Spooren J, et al. NMR evidence of a sharp change in a measure of local order in deeply supercooled confined water. Proc Natl Acad Sci USA. 2008; 105 (35): 12725–9. doi: 10.1073/pnas.0805032105

50. Marcus Y. The standard partial molar volumes of ions in solution. Part 4. Ionic volumes in water at 0–100 °C. J Phys Chem B. 2009; 113 (30): 10285–91. doi: 10.1021/jp9027244

51. Marcus Y. Ionic volumes in solution. Biophys Chem. 2006; 124 (3): 200–7. doi: 10.1016/j.bpc.2006.04.013

52. Li J, Zhang H-F, Shao G-Q, Wu B-L, Ouyang S-X. Negative differential resistance: another banana? Europhys Lett. 2014; 108 (2): 27005. doi: 10.1209/0295-5075/108/27005

53. International Association for the Properties of Water and Steam. R15-11: Release on the IAPWS formulation 2011 for the thermal conductivity of ordinary water substance. 2011. Available from: https://iapws.org/technical-guidance/release/ThCond

54. International Association for the Properties of Water and Steam. R12-08: Release on the IAPWS formulation 2008 for the viscosity of ordinary water substance. 2008. Available from: https://iapws.org/technical-guidance/release/viscosity

55. Mills R. Self-diffusion in normal and heavy water in the range 1–45°. J Phys Chem. 1973; 77 (5): 685–8. doi: 10.1021/j100624a025

56. Harris KR, Woolf LA. Pressure and temperature dependence of the self-diffusion coefficient of water and oxygen-18 water. J Chem Soc Faraday Trans 1. 1980; 76: 377–85. doi: 10.1039/F19807600377

57. Prielmeier FX, Lang EW, Speedy RJ, Lüdemann H-D. The pressure dependence of self diffusion in supercooled light and heavy water. Ber Bunsenges Phys Chem. 1988; 92 (10): 1111–7. doi: 10.1002/bbpc.198800282

58. International Association for the Properties of Water and Steam. R1-76(2014): Revised release on the surface tension of ordinary water substance. 2014. Available from: https://iapws.org/technical-guidance/release/Surf-H2O

59. Okur HI, Drexler CI, Tyrode E, Cremer PS, Roke S. The Jones–Ray effect is not caused by surface-active impurities. J Phys Chem Lett. 2018; 9 (23): 6739–43. doi: 10.1021/acs.jpclett.8b02957

60. Petersen PB, Johnson JC, Knutsen KP, Saykally RJ. Direct experimental validation of the Jones–Ray effect. Chem Phys Lett. 2004; 397 (1–3): 46–50. doi: 10.1016/j.cplett.2004.08.048

61. Craig VSJ, Ninham BW, Pashley RM. Effect of electrolytes on bubble coalescence. Nature. 1993; 364 (6435): 317–9. doi: 10.1038/364317a0

62. Craig VSJ, Ninham BW, Pashley RM. The effect of electrolytes on bubble coalescence in water. J Phys Chem. 1993; 97 (39): 10192–7. doi: 10.1021/j100141a047